Booster Fly-Back Analysis of Reusable Launch Systems

Çavdar, I.; Mooij, E.

DOI
10.2514/6.2024-1458

Publication date
2024

Document Version
Final published version

Published in
Proceedings of the AIAA SCITECH 2024 Forum

AIAA SciTech Forum
8-12 January 2024, Orlando, FL
AIAA SCITECH 2024 Forum

10.2514/6.2024-1458

Booster Fly-Back Analysis of Reusable Launch Systems

Irmak Cavdar* and Erwin Mooij †
Delft University of Technology, Faculty of Aerospace Engineering,
Kluyverweg 1, 2629 HS Delft, The Netherlands

Within the last decade, the use of launch vehicles has increased as private companies have emerged in the space exploration industry. Compared to the early 1980s, the market for launch vehicles has become significantly more competitive, introducing the desire to have fully reusable launch vehicles. The true benefits of fully reusable launch vehicles can only be achieved once both stages are fully operational and recoverable. This stimulates the need for a comprehensive mission design. In this paper, this is achieved by revisiting the mission profiles of flyback boosters. An extensive analysis of the design-space is performed to identify the contributions of each decision variable to the trajectory design. The results concluded that such an approach supports achieving a more efficient optimization, with better convergence speed and solution performance.

I. Introduction

In the pursuit of advancing space exploration, the development of fully reusable launch vehicles introduced a paradigm shift in the aerospace industry. Previously, the major hurdle to developing a fully reusable launch vehicle was the significant development costs of such a system. As the operational benefits of the vehicles became unjustifiable against the complexity and cost of the design, various missions, such as the Space Shuttle by the National Aeronautics and Space Administration (NASA) or the Liquid Flyback Booster by the German Aerospace Center (DLR), were terminated at early stages.[13] Nevertheless, the operational cost of current launch vehicles, such as Ariane and Delta, are non-negligible due to the refurbishment and expandability costs before the launch. A successful development of a reusable launch vehicle can decrease the time associated with vehicle design and launch costs in the long run.[6]

Among various approaches to fully reusable launchers, a flyback booster, complemented by the emerging importance of spaceplanes, stands out as a viable solution. Due to their ability to land horizontally, just like a conventional aircraft, spaceplanes offer unique advantages for the development of flyback boosters. The Future European Space Transportation Investigation Programme (FESTIP) was a study between 1994 and 1999 that evaluated 16 different reusable launcher concepts. An analysis at a sufficient level of detail, many of which beyond a conceptual level, was performed for each vehicle, such that the technological challenges of these systems could be evaluated. After an iterative design process, the FESTIP System Study Concept 16 (FSSC-16) was identified as one of the two feasible designs with possible growth potential.

FSSC-16 was a two-staged vehicle that had a step-wise system development. The first FSSC-16 design had a reusable booster and an Ariane-5 core stage. The improved version had a reusable booster and a reusable orbiter, creating a fully reusable launch vehicle design. In this setup, both the orbiter and the booster were designed to be winged bodies. The choice of a winged vehicle was especially significant for the booster stage. This ensured that the capabilities of a suborbital spaceplane can be adapted by the booster stage, giving it increased operational flexibility compared to other conventional first-stage boosters. This operational flexibility can reduce the turnaround time, as well as the cost of transportation from the landing site to the launch site. SpaceX has already pioneered the concept of recoverable boosters. However, their

*MSc Student, Section Astrodynamics and Space Missions, irmakcavdar@gmail.com. Currently: GNC Engineer at Dawn Aerospace
†Associate Professor, Section Astrodynamics and Space Missions, e.mooij@tudelft.nl, Associate Fellow AIAA.

Table 1. FSSC-16 Booster Properties[1]

m [kg]	L_{ref} [m]	h_{ref} [m]	w_{ref} [m]	b_{ref} [m]	c_{ref} [m]	S_{ref} [m^2]
57,000	40.0	6.6	6.4	21.8	18.63	405.6

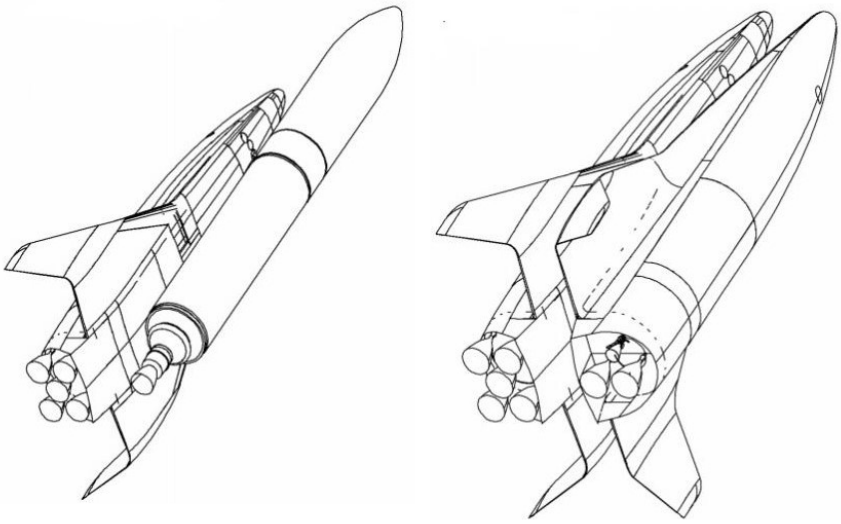

Figure 1. FSSC-16 semi-reusable with Ariane 5 core stage (left) and FSSC-16 the fully reusable concept (right)[3]

research is focused on vertical rocket landing with means of propulsive systems. Meanwhile, a hybrid system with combined aerodynamic and propulsive capabilities, such as FSSC-16, still needs to be analyzed.

To ensure that the fly-back capabilities of a flyback booster outweighs the development costs, both the system's capabilities and the mission profile have to be revisited. By conducting a detail study on the trajectory and understanding the engineering principles behind a powered fly-back trajectory, this paper aims to contribute to the advancement of reusable launch technologies. The knowledge attained from this research can lead to improvements in performance, cost, and safety of flyback boosters, making space more accessible and sustainable for various endeavors.

II. The Flyback Problem

A. Reference Vehicle

The selected reference vehicle for the assessment of the fly-back capabilities was designed during the FESTIP study. FSSC-16 aimed to identify the required level of technological development for Europe to utilize fully reusable launch vehicles. As a result, in 1999 a preliminary study was completed at a system level and concluded that FSSC-16 has a growth potential with mission flexibility. The booster stage of the FSSC-16 is a powered vehicle that is equipped with four air-breathing engines to be used during the cruise flight back to the launch site. After separation from the second stage, the booster can be controlled by aerodynamic surfaces and the thrust force. Table 1 introduces the vehicle characteristics, meanwhile Figure 1 shows the step-wise approach of FSSC-16 with the initial and final operational configurations.

Although FESTIP provided a preliminary overview of the FSSC-16 vehicle and its characteristics, certain aspects are missing. A complete aerodynamic database of the orbiter or the booster is one of these aspects. Therefore, since the booster has a close resemblance to HORUS, the original second stage of the Saenger Two-Stage-To-Orbit concept analyzed in the 1980s and 1990s, the aerodynamic model is adapted from the HORUS database according to the new reference area and center of mass of the FSSC-16 orbiter.[9] It is worthwhile to mention that the booster consists of aerodynamic control surfaces, which are a bodyflap, two elevons, and two rudders. As these are utilized for sustaining the pitch stability of the vehicle, the

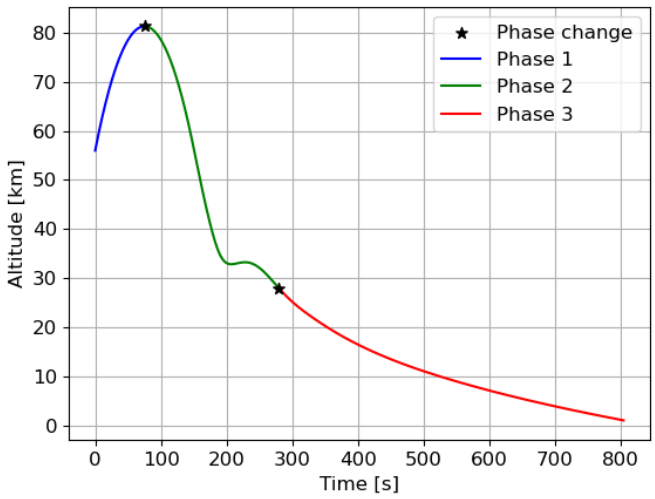

Figure 2. Altitude profile of a reference return flight of the FSSC-16 flyback booster

aerodynamic databases of the control surfaces are also adapted. Meanwhile, the mass model is defined considering that the vehicle is a non-elastic body with varying mass properties due to fuel consumption.

B. Mission Profile

The return flight of the booster was broken down to three main phases.

1. **Phase 1 Ballistic Trajectory:** Phase 1 initiates with a stage separation at an altitude of 56 km and at Mach 6.5, and ends when the vehicle reaches a flight-path angle of 0°. Immediately after separation the flyback booster remains at its high velocity from the separation. Due to the inertia of the vehicle and high speed, the flyback booster enters a ballistic trajectory, as depicted in Figure 2, with an increasing altitude between 0 and 70 seconds. Phase 1 is the ascent of this ballistic trajectory. While the flyback booster is ascending, the atmosphere with density keeps decreasing. As a result, the vehicle will experience a lower dynamic pressure, and consequently a lower lift. This is significant to note as it limits the aerodynamic capabilities of the vehicle, and as such it will be less responsive to steering commands, *i.e.*, the angle of attack, α, and bank angle, σ, commanded by the guidance system.

2. **Phase 2 Turn Maneuver:** After this peak point, in which $\gamma = 0°$, as the vehicle starts gaining lift, the second phase begins. After the launch and during Phase 1, the vehicle is flying away from the landing site. During Phase 2, the vehicle has to initiate the return to the launch site. To achieve that, first the heading angle of the vehicle has to be corrected. Thus, the vehicle performs a turn maneuver to obtain a final heading angle of $-70°$.

3. **Phase 3 Fly Back to Launch Site:** Phase 3 begins as soon as the vehicle obtains the desired heading angle. Depending on the energy of the booster, either a powered or unpowered flight is performed until the Terminal Area Energy Management (TAEM) condition of 0.75° of distance-to-go is reached. The vehicle must sustain its desired heading angle and have sufficient energy to successfully enter the terminal area.

III. Flight Dynamics

To review potential instabilities and response characteristics, it is to formulate the flight dynamics of a vehicle. This analysis is first conducted by identifying the external forces and equations of motion. Later on, to showcase the pitch stability of the booster, external moments are presented.

A. External Forces and Equations of Motion

A vehicle that is performing a powered return flight encounters three main forces of aerodynamic, gravitational, and propulsive origin. The aerodynamic force is expressed in the aerodynamic reference frame, identified by index A, and consists of drag D, side force S, and lift L:

$$\boldsymbol{F_{A,A}} = -\begin{pmatrix} D \\ S \\ L \end{pmatrix} = -\begin{pmatrix} C_D \bar{q} S_{ref} \\ C_S \bar{q} S_{ref} \\ C_L \bar{q} S_{ref} \end{pmatrix} \tag{1}$$

in which S_{ref} indicates the aerodynamic reference area in m^2. Furthermore, the forces are dependent on respective force coefficients C_D, C_S, and C_L. Usually, C_D and C_L, are a function of Mach number, M, and angle of attack, α. C_S is a function of M and side-slip angle, β.

Furthermore, $\bar{q} = \frac{1}{2}\rho V^2$ is the dynamic pressure that is dependent on the atmospheric density ρ, in $\mathrm{kg/m}^3$, and airspeed V. The gravitational force is commonly defined in the NED reference frame as $\boldsymbol{F}_{g,v} = m(g_N \ 0 \ g_D)^T$, whereas the thrust force is represented in the propulsion reference frame, index P, as $\boldsymbol{F_{T,P}} = (T \ 0 \ 0)^T$

Here, T is expressed as:

$$T = I_{sp} g_0 \dot{m} \tag{2}$$

Consequently, the full set of equations of motion of the translational motion for a body that is subjected to mass m changes and under influence of aerodynamic, propulsive and gravitational forces is identified by.[8] The mathematical representation in the spherical coordinates is as follows:

$$\dot{V}_g = \frac{F_V}{m} + \omega_{cb}^2 R \cos\delta \left(\sin\gamma_g \cos\delta - \cos\gamma_g \sin\delta \cos\chi_g\right) \tag{3}$$

$$\begin{aligned} V_g \dot{\gamma}_g = \ & \tfrac{F_\gamma}{m} + 2\omega_{cb} V_g \cos\delta \sin\chi_g + \tfrac{V_g^2}{R} \cos\gamma_g + \\ & + \omega_{cb}^2 R \cos\delta \left(\cos\delta \cos\gamma_g + \sin\gamma_g \sin\delta \cos\chi_g\right) \end{aligned} \tag{4}$$

$$\begin{aligned} V_g \cos\gamma_g \dot{\chi}_g = \ & \tfrac{F_\chi}{m} + 2\omega_{cb} V_g \left(\sin\delta \cos\gamma_g - \cos\delta \sin\gamma_g \cos\chi_g\right) \ + \\ & + \ \tfrac{V_g^2}{R} \cos^2\gamma_g \tan\delta \sin\chi_g + \omega_{cb}^2 R \cos\delta \sin\delta \sin\chi_g \end{aligned} \tag{5}$$

where F_v, F_γ, and F_χ are defined as:

$$\begin{aligned} F_V = & - D + T\cos\alpha_g \cos\beta_g \cos\psi_T \cos\epsilon_T + T \sin\beta_g \sin\psi_T \cos\epsilon_T - T \sin\alpha_g \cos\beta_g \sin\epsilon_T \ + \\ & - mg_d \sin\gamma_g + mg_n \cos\gamma_g \cos\chi_g \end{aligned} \tag{6}$$

$$\begin{aligned} F_\gamma = & -(S + T\cos\alpha_g \sin\beta_g \cos\psi_T \cos\epsilon_T - T \ cos\beta_g \sin\psi_T \cos\epsilon_T - T \sin\alpha_g \sin\beta_g \sin\epsilon_T) \sin\sigma_g \ + \\ & + \ (L + T\sin\alpha_g \cos\psi_T \cos\epsilon_T + T\cos\alpha_g \sin\epsilon_T) \cos\sigma_g \ + \\ & - \ mg_d \cos\gamma_g - mg_n \sin\gamma_g \cos\chi_g \end{aligned} \tag{7}$$

$$\begin{aligned} F_\chi = & -(S + T\cos\alpha_g \sin\beta_g \cos\psi_T \cos\epsilon_T - T\cos\beta_g \sin\psi_T \cos\epsilon_T - T \sin\alpha_g \sin\beta_g \sin\epsilon_T) \cos\sigma_g \ + \\ & - \ (L + T\sin\alpha_g \cos\psi_T \cos\epsilon_T + T\cos\alpha_g \sin\epsilon_T) \sin\sigma_g \ + \\ & - \ mg_n \sin\chi_g \end{aligned} \tag{8}$$

The accompanying kinematic equations are:

$$\dot{R} = \dot{h} = V \sin\gamma \tag{9}$$

$$\dot{\tau} = \frac{V \sin\chi \cos\gamma}{R \cos\delta} \tag{10}$$

$$\dot{\delta} = \frac{V \cos\chi \cos\gamma}{R} \tag{11}$$

$$\dot{m} = \frac{T}{I_{sp} g_0} \tag{12}$$

B. External Moments and Trim Analysis

As the forces that are identified above are not exerted at the center of mass, they induce a moment around this point. As a pitch trimmed point mass motion is analyzed for this study, moment due to external forces are expressed as below:

$$\boldsymbol{M_{A,A}} = C_m \bar{q} S_{ref} c_{ref} \tag{13}$$

$$\boldsymbol{M_{T,B}} = M_{P,y} \tag{14}$$

Since a concrete trim logic was not identified by the FESTIP study, the trim law of HORUS is adopted. The trim condition is achieved when the total pitch moment coefficient C_m is equated to be zero by deflecting the aerodynamic control surfaces, bodyflap and elevons. Accordingly, the trim condition is mathematically defined by the equation below:

$$C_m = C_{m_0} + \Delta C_{m_b} + 2 \cdot \Delta C_{m_e} \tag{15}$$

It is worthwhile to mention that the aerodynamic database used for this study is for Mach numbers that are higher than 1.2. Therefore, the vehicle's trim capability is not assessed after Mach 1.2. During the simulation, the aerodynamic control surfaces, bodyflap and elevons, are left at their final position. The logic behind trim algorithm is as follows. While M is larger than 5, for current α and M the corresponding body-flap moments are evaluated as a function of deflection. Through inverse interpolation, the deflection angle that is corresponding to the current moment is identified. Whereas, when M is smaller than 5, the elevons are deflected alongside the body-flap.

In the current application, the trim logic is developed using the reference trajectory that was provided by the FESTIP study. In Figure 3, the deflection angles and the corresponding total pitch moment of the vehicle is depicted. The elevons are inactive until the Mach number is below 5. At the point where the bodyflap reaches its maximum deflection of $-20°$ and gets saturated, the elevons are activated. Note that the bodyflap is only utilized for aerodynamic trim. Since the elevons are also used to control the vehicle, it is not desired to saturate the elevons and have maximum deflection only with trimming. Thus, the algorithm was designed to reach the trim condition by using 50% of the deflection capabilities of the elevons, between $[-20°, 20°]$

IV. The Flyback Trajectory Problem

A. Problem Description

The problem at hand is formulated as a multi-objective optimization, with the objectives being the minimum fuel consumption and minimum root sum square (RSS) of the path constraint violations. Minimum fuel consumption during the fly-back flight would allow more fuel to be consumed for the launch phase, increasing the efficiency of the launcher. The second objective of the optimization is to minimize the RSS of path-constraint violations, as surpassing the path constraints pose structural and operational challenges for the booster. The RSS of the normalized path constraints is calculated as below:

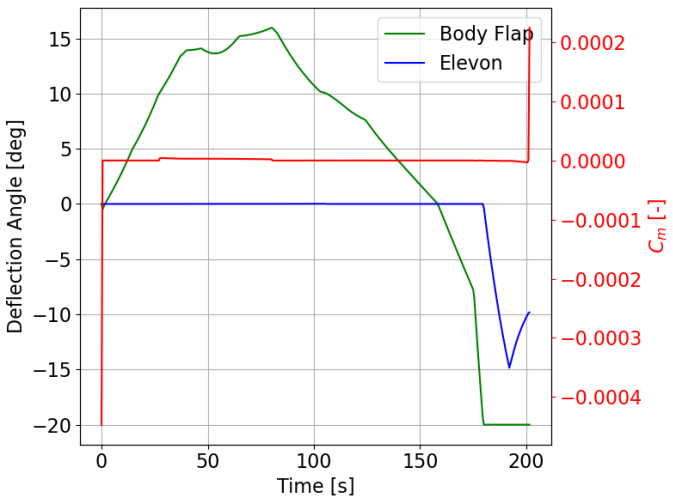

Figure 3. Deflection angles of the FSSC-16 control surfaces during the trim

$$RSS_{constraints} = \sqrt{\sum_{i=1}^{n} \left(\frac{x_i - C_i}{C_i} \right)^2} \tag{16}$$

in which x_i refers to the current value of the constraint and C_i is the limit value for the constraint. The associated cost function is identified as:

$$\min \left(J_{FC}, J_{RSS} \right) \tag{17}$$

Note that the fuel consumption function is assessed based on the remaining fuel mass:

$$M_{FC} = \min \left(M(t_0) - M(t_f) \right) \tag{18}$$

in which M_{FC} refers to the mass of the consumed fuel, $M(t_0)$ is the initial mass, and $M(t_f)$ is the mass when the simulation is terminated.

The constraints that are accounted for in this objective function are the g-load constraint, heat flux constraint, and trim violation constraint, which are identified as the path constraints.

- Maximum heat flux: $q_c = 93$ kW/m^2
- Maximum g-load: $n_g = 3$g
- Maximum trim violation: $t_T = 0$ s

in which the maximum g-load is calculated by retrieving the acceleration history from the simulation, dividing by gravitational acceleration g, and calculating the maximum value. Mathematically, the g-load is calculated as:

$$n_g = \frac{a_a + a_T + a_g}{g} \tag{19}$$

in which a_a refers to aerodynamic acceleration, a_T refers to thrust acceleration, and a_g is the gravitational acceleration. Furthermore, the max heat flux is calculated using Chapman's Equation:

$$q_c = c_1 \frac{1}{R_N^n} \rho^{1-n} V^m \tag{20}$$

in which $n = 0.5$ for laminar boundary layer, R_N is the nose radius of the vehicle, m is an empirical constant which is often taken as $m = 3$. The maximum trim violation is calculated as follows. As long as the vehicle is

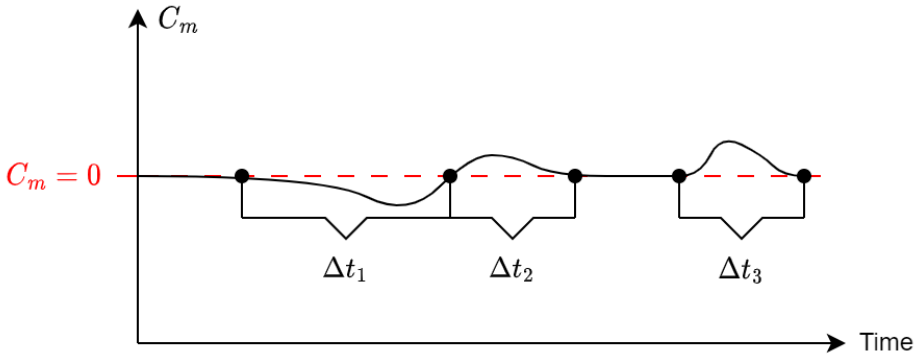

Figure 4. Total pitch moment coefficient vs. time graph to visualize the trim violation condition

above Mach 1.2, it is desired to have a trimmable trajectory. Therefore, for $20 > \mathrm{M} > 1.2$, the trim violation is calculated such that for the duration in which the total pitch moment coefficient C_m is not zero is added up. For instance, the trim violation constraint in Figure 4 is calculated as:

$$t_T = \Delta t_1 + \Delta t_2 + \Delta t_3 \tag{21}$$

A second set of constraints is posed on the control system. Although this study does not include attitude control, it aims to obtain a more realistic trajectory by accounting for certain control constraints. As the vehicle's control system governs physical components on the vehicle, it is imperative to acknowledge the existence of inherent limitations on the deflection capabilities of the control surfaces. The control constraints are defined as below:

- Maximum angle of attack rate: $\dot{\alpha} = 10$ deg/s
- Maximum bank angle rate: $\dot{\sigma} = 10$ deg/s

The last constraint concerns the termination condition. The only boundary is the final distance-to-go of 0.75°. The constraint aims to guide the design space towards solutions that reach the TAEM phase. For optimization algorithm to account for the constraints, a penalty function is introduced:

$$Penalty = \sum_{i=1}^{n} \left(\frac{x_i - C_i}{C_i} \right) \cdot k_1 \tag{22}$$

where k_1 is a constant. Depending on the original value of the objective, the original value of the constraint and the severity of the constraint, k_1 is chosen through trial and error. The penalty function essentially identifies the degree of the constraint violation.

The last component to formulate the fly back problem to a mathematical problem consists of the decision variables. At each optimization, a set of decision variables are output for each optimum trajectory. The output vector subsequently serves as the primary source for guidance commands to the vehicle, forming the basis of the guidance logic. The decision variables are:

$$\mathbf{x}_{powered} = \begin{bmatrix} T & \epsilon_T & \psi_T \end{bmatrix}^T \tag{23}$$

in which T is the thrust magnitude, ϵ_T is the thrust elevation angle, and ψ_T is the thrust azimuth angle. The aerodynamic guidance parameters, angle of attack α and bank angle σ, are not considered as decision variables for the powered vehicle. Instead, the booster follows a pre-defined α and σ profile. The objective is to choose an α profile in which the vehicle is always trimmable, comparable to the reference profile. This approach ensures compliance with the trim constraint while concurrently diminishing the problem's dimensionality by following a pre-defined profile. This aspect becomes particularly significant when conducting iterative simulations for the purpose of exploring and optimizing the design space. Nevertheless, note that the trimmability is still affected by the thrust force, thus requires an evaluation.

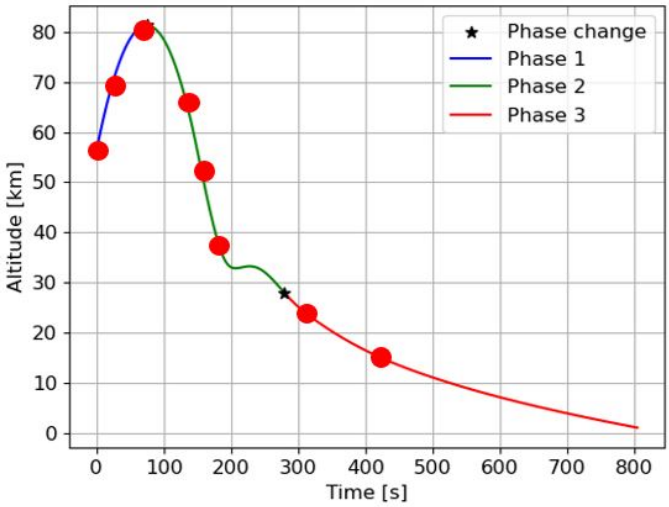

Figure 5. Control nodes (indicated by red dots) along a reference trajectory

The reference bank angle profile is obtained from literature on flyback boosters.[10,13] During Phase 1, the vehicle is performing a maneuver to roll around its x_B axis to orient itself correctly. Therefore, it comes out of the inverted configuration and changes in to the conventional re-entry configuration. In Phase 2, the bank angle profile is adapted such that a turning flight is performed, within the limits of the g-load constraint. Finally, from the reference mission, it is expected to observe a cruise flight which is around 15 km altitude at Phase 3. The cruise condition is desired to be maintained to sustain a leveled flight with a desired heading angle. Due to couplings in the flight dynamics, especially the yaw and roll coupling, the heading angle control is achieved through controlling the bank angle. The pre-defined bank angle profile is expressed as:[13]

$$\sigma = k_{heading}\left[\left(-\arctan\left(\frac{\delta-\delta_t}{\tau-\tau_t}\right)-\frac{\pi}{2}\right)-\chi\right] \tag{24}$$

in which δ and τ are the latitude and longitude, respectively and the subscript t refers to the target point, which is the landing site, χ is the current heading angle and $k_{heading}$ is the controller gain, which is equal to $k_{heading} = 0.15$.

B. Node Control Method

To control the vehicle and make sure that the reference flight profile is followed by the vehicle, a node control method is implemented. Each node contains a decision variable vector and is located at a certain point that is identified with an independent variable. Since the flyback booster is powered, variables were lacking to show a monotonically increasing or decreasing trend for the entire of the flight. Therefore, up until the end of Phase 1, the independent variable is identified as the flight-path angle γ, since it is constantly reducing until the peak altitude point. For Phase 2 and Phase 3, the independent variable is set to be the altitude. At each node the decision variables are re-introduced by the values set by the user. The entire flight profile is simulated with multiple nodes that are connected by a Hermite spline interpolation. At each node the decision variables identified in Equation 23 are interpolated.

Various studies concluded that 18 optimization variables are efficient for the optimization speed and result quality.[11] Notably, each node in this context encompasses three thrust variables, amounting to a maximum of six nodes. Meanwhile, in the context of missions involving distinct phases, prior studies have similarly suggested that the utilization of up to six nodes suffices for effective control of each individual phase.

Taking these results under consideration, eight nodes are placed along the trajectory. Since Phase 1 is a relatively quick phase, due to the forces on the booster, it is decided to control this phase with 3 nodes. The remaining 5 nodes are placed along Phase 2 and Phase 3. Note that the third node of Phase 1 is

placed at the peak point of the ballistic flight, to ease the transition between the independent variables. This approximately corresponds to 80 km, although the exact value is dependent on the thrust parameters at Phase 1. The remaining nodes are placed depending on the altitude value of the final node. Literature suggests that around 10 km altitude the vehicle begins to control its altitude and bank angle to sustain the cruise conditions, a final node is placed at this point to control the trajectory until the desired final distance-to-go of 0.75° is reached.[13]

C. Design Space Exploration Methodology

To achieve the three benefits of a flyback booster, which are reduced cost, sustainability, and accessibility to space, it is necessary to obtain a flyback booster that is operable. To achieve such a system, a reliable vehicle and trajectory design has to be performed. This paper focuses on the trajectory design aspect. Since a detailed trajectory design is an intricate task that requires elegant analysis of the parameters that influence the trajectory, it is aimed to obtain the relationship between the trajectory and design parameters in an efficient manner.

Design space exploration allows for a systematic analysis between the parameters of interest and the results, i.e, the trajectory. Each design-space exploration method provides information on the relationship at different levels. Key methodologies that are considered for analyzing the design space are identified below. Note that the results of each method is statistically quantified and compared using Analysis of Variance (ANOVA).

One-at-a-time Simulation and Monte Carlo Analysis

One-at-a-time simulation and Monte Carlo analysis are two methods that are preferred for preliminary identification of the design space. Identifying the effect of a single decision variable on the entire trajectory is the first step in understanding the relationship between the decision variables and the trajectory. After identifying the basic sensitivity, a Monte Carlo analysis can be used to understand the impact of simultaneously varying multiple inputs on a model's response.

In case where a substantial number of parameters are varied, it is possible to encounter interactions between different parameters. This arises from the fact that a design choice made at one specific point along the trajectory may exert an influence on subsequent design choices. In the absence of prior knowledge on the model dynamics, Monte Carlo analysis cannot be used to identify the interactions between different parameters. Such an approach is not only inadequately structured, but also necessitates complex post-processing procedures. The excessive data to be post-processed, could pose challenges in deriving coherent conclusions regarding the relationship between the model and its parameters. Consequently, one-at-a-time simulation is only used to define the initial range of the decision variables, which is $[0, 400]$ kN for thrust magnitudes and $[0°, 60°]$ for thrust angles at all nodes.

Full and Fractional Factorial Design

A method for a more structured design-space exploration is a factorial design approach. In a full factorial design, all the decision variables, or the factors, are varied at the same time to study the interactions between factors. Given k number of factors, investigating all combinations at m levels is called a factorial design. For such a case, m^k is the total number of simulations to execute. In case there are 2 levels, i.e, the minimum and maximum value, for 2 factors, the design matrix is expressed as:

$$L_4 = \begin{bmatrix} -1 & -1 \\ 1 & -1 \\ -1 & 1 \\ 1 & 1 \end{bmatrix} \tag{25}$$

in which -1 refers to the minimum and 1 refers to the maximum value of the factor. For each column a percentage contribution to the total variance can be established with ANOVA. Since columns are attributed to a factor, through ANOVA each factor's percentage contribution is calculated. As the number of levels increased, a wider range of potential conditions can be captured. Consequently, with the captured conditions, there is a higher chance of observing the full variability of the response.

However, if the number of factors is large, number of factor combinations grow. For instance, regarding the powered flyback booster problem with 24 factors, even with 2 levels the total number of possible combinations amounts to $2^{24} = 16,777,216$. Assuming each simulation takes around one second, executing all the combinations would take 195 days. Given the computational resources and time that would be spent while running them all, it is not efficient to conduct a full factorial design for this research.

Nevertheless, it is possible to assess a subset of all possible combinations. Such a method is called the fractional factorial design (FFD). A fractional factorial design copes with the problem by selecting a subset of the factorial design space. However, the method combines certain factors and interactions into a single effect to be able to reduce the number of simulations. This introduces a confounding, which refers to the situation when certain effects cannot be distinguished from one another. The severity of the confounding effect is determined by the chosen design matrix.

Fractional Factorial Design and Methodology

Due to the nature of fractional factorial design, variations in the interactions are confounded with variations of the factors. To cope with this problem, no factor should be assigned to columns that indicate interactions in the design matrix. These so-called "interaction columns" follow from literature.[5] As it is not arbitrary to decide which columns to leave empty, the decision is associated with the level of confounding. This assessment is performed through interactions tables. The data obtained from this table are employed to systematically allocate the factors to specific array columns.

Table 2. Interaction table for the L_8 array

	1	**2**	**3**	**4**	**5**	**6**	**7**
1		3	2	5	4	7	6
2			1	6	7	4	5
3				7	6	5	4
4					1	2	3
5						3	2
6							1

The interaction table for an L_8 array is presented in Table 2 [a]. Looking at the table it can be seen that the interaction between column 1 and column 2 can be found in cell (1, 2). The value in cell (1, 2) suggest that column 1 and column 2 are confounded with column 3. If decision variables A_1, A_2, and A_3 are assigned to columns 1,2, and 3, respectively, the interaction between A_1 and A_2 cannot be studied independent of A_3. If it is believed or suspected that the interaction between A_1 and A_2 is significant then the dependence should be broken by not assigning any factor to column 3. This decreases the confounding and allows the main effects to be analyzed more efficiently.

Given the computational and coding complexities, an L_{32} matrix with Resolution IV is chosen as a feasible option for this research. In Resolution IV L_{32} array, seven factors can be analyzed with minimal two-way interactions. In this case, a two-way interaction refers to interaction between two factors.

The 24 decision variables are analyzed in subsets of 7. Out of 32 columns of an L_{32} array, the factors to be analyzed are assigned to columns 1, 2, 4, 7, 8, 16, and 29. While the percentage contribution of these columns represents the main effects, the rest of the columns represent the interactions. Note that within the rest, columns 3, 5, and 6 are the columns that have confounded interactions. Knowing the exact distribution of the interactions, an analysis can be performed in a more structured manner. However, if interactions with high impact are represented in columns 3, 5, and 6, then there could be a confounding effect that has to be regarded. This can be assessed by swapping the column location of factors within a subset. Therefore,

[a] An L_8 array has 7 columns (to be used to assign factors) and 8 rows (which refers to number of combinations that are studied).

if factor A is assigned to column 1, in the next round factor A is assigned to column 16 while keeping the same factors but also changing their column location. If the original subset and the column-swapped subset yield similar amount of percentage contributions, then it can be concluded that the subset is not suffering from any confounding effects.

Methodology

A brief step-by-step guideline for the methodology is as follows. Different subsets are generated to analyze the contribution of parameters to variability of the response. Afterwards, the thrust parameters within a subset are assigned to different columns. The subsets that are generated with this method are identified as Subset-n Swapped Column, in which n refers to an independent number chosen to identify the subset.

An ANOVA analysis is conducted to assess the percentage contribution of the thrust parameters and the interactions within a subset. The next subsets are generated using the thrust parameters that are either had the highest individual contribution or the highest interactions. In the meantime, the standard deviation, variance, and mean of the subsets are also assessed. The variance provides information on to what extent the data is distributed around the mean value. Therefore, a subset with a high variance indicates that the interactions of the individual thrust parameters influence the response more than a subset with a lower variance. If a subset has a significantly low variance, even though it has high contributions such as 70% it will be negligible compared to others.

Valuable insights can be obtained by analyzing the variance and mean simultaneously. A high set of values indicate that the factors within the subset have a wide range of effect on the response. This suggests that the interactions between these factors could be significant. Conversely, low values for both variance and mean imply a lower contribution of the subset to the response. In this scenario, the effect of factors may either be statistically insignificant, a determination that can be validated through percentage contributions, or the interactions may exhibit consistency.

V. Fractional Factorial Design Results

A. Fuel Consumption

To sustain a leveled flight, at Phase 3, the booster has to pull up the nose of the vehicle. Consequently, the drag and gravity force has to be overcome at the final nodes. Increasing the thrust force could be a feasible solution for this. However, increasing thrust yields a higher acceleration, which increases the vehicle's velocity. As the velocity increases, the drag is increased exponentially, introducing a non-linear relationship between the two. Therefore, although a constant fuel flow demonstrates a linear relationship with the fuel consumption, complex aerodynamic effects may induce non-linearities. To have a comprehensive analysis, the design space exploration is conducted. It is worthwhile to note that the fuel consumption is normalized with respect to the flight time, so that a comparison is carried out without being concerned about the influence of the duration between two consecutive node.

Subset-6, characterized by the smallest mean and variance, indicates that thrust parameters within this set have a comparatively minor impact on response variability compared to other subsets, notably Subset-2 with the highest mean. Responses within Subset-6 consistently cluster around a low mean value. The results yield that the individual contribution of the thrust elevations are not sufficient to explain the variability of the fuel consumption.

The values of Subset-6 concludes that the interaction between elevation angles at different nodes is insignificant. However, it is worthwhile to mention that, by only looking at Subset-6 it is not possible to conclude whether all the thrust elevation interactions are insignificant. Such a conclusion can be made, once the subset includes both the thrust elevation angle and another thrust parameter, such as the thrust magnitude. Hence, the Subset-7 and Subset-8 are generated. Looking at the mean value of the Subset-7, it is noticed that the value is comparable to the mean of Subset-2. This suggests that, the central tendency and the dispersion of the two subsets are similar. Analyzing the data obtained from the two, it can be observed that when thrust elevation angles are coupled with thrust magnitudes, the variability of the response is increased.

An important behavior is spotted once the mean and variance of the subsets, and the corresponding swapped column subsets are analyzed. For each of the original and the swapped-column subset, the mean and variance are almost identical. A difference can be observed in the fourth decimal place. When these

Table 3. Properties of selected fractional factorial subsets of the fuel consumption

	Parameters	Mean	STD	Variance
Subset-1	$T_1 - T_2 - T_3 - T_4 - T_5 - T_6 - T_7$	1.6964	0.4557	0.2076
Subset-1 Swapped Column	$T_3 - T_2 - T_4 - T_6 - T_7 - T_1 - T_5$	1.6968	0.4554	0.2074
Subset-2	$T_2 - T_3 - T_4 - T_5 - T_6 - T_7 - T_8$	1.7567	0.6625	0.4389
Subset-2 Swapped Column	$T_6 - T_4 - T_8 - T_2 - T_7 - T_5 - T_8$	1.7560	0.6617	0.4379
Subset-6	$\epsilon_1 - \epsilon_2 - \epsilon_3 - \epsilon_4 - \epsilon_5 - \epsilon_6 - \epsilon_7$	1.2039	0.0137	0.0002
Subset-7	$T_2 - T_3 - T_7 - T_8 - \epsilon_3 - \epsilon_7 - \epsilon_8$	1.7158	0.6415	0.4116
Subset-7 Swapped Column	$\epsilon_8 - T_2 - T_7 - \epsilon_3 - T_8 - T_3 - \epsilon_7$	1.7157	0.6418	0.4119
Subset-8	$T_2 - T_3 - T_5 - T_8 - \epsilon_2 - \epsilon_5 - \epsilon_8$	1.6924	0.5773	0.3333
Subset-8 Swapped Column	$T_5 - \epsilon_8 - \epsilon_2 - T_3 - \epsilon_5 - T_8 - T_2$	1.6926	0.5769	0.3329

Table 4. Properties of selected fractional factorial subsets of the final distance-to-go

	Parameters	Mean	STD	Variance
Subset-1	$T_1 - T_2 - T_3 - T_4 - T_5 - T_6 - T_7$	5.6450	0.6955	0.4838
Subset-1 Swapped Column	$T_5 - T_3 - T_4 - T_7 - T_1 - T_2 - T_6$	5.6470	0.6977	0.4867
Subset-2	$T_2 - T_3 - T_4 - T_5 - T_6 - T_7 - T_8$	5.6578	0.8178	0.6687
Subset-2 Swapped Column	$T_4 - T_8 - T_6 - T_7 - T_3 - T_5 - T_2$	5.6610	0.8216	0.6750
Subset-4	$T_1 - T_2 - T_3 - T_4 - T_5 - T_6 - T_8$	5.5517	0.7459	0.5564
Subset-4 Swapped Column	$T_6 - T_2 - T_8 - T_4 - T_1 - T_5 - T_3$	5.5530	0.7430	0.5520
Subset-6	$T_2 - T_3 - T_4 - T_7 - \epsilon_2 - \epsilon_3 - \epsilon_7$	5.5294	0.6612	0.4379
Subset-6 Swapped Column	$\epsilon_3 - T_4 - \epsilon_2 - T_3 - \epsilon_7 - T_2 - T_7$	5.5269	0.6480	0.4199
Subset-11	$T_2 - T_3 - T_7 - T_8 - \psi_2 - \psi_3 - \psi_7$	5.8082	1.2474	1.5561
Subset-11 Swapped Column	$T_8 - \psi_7 - T_3 - \psi_2 - T_2 - \psi_3 - T_7$	5.7892	1.2986	1.6863

values are identical, regardless of the column assignment, it is feasible to conclude that there are minimal interactions between the factors that are present in the subset.

B. Final Distance-to-go

The same subset methodology as before is used for analyzing the final distance-to-go. Note that the contents of the subsets shows variety, except Subset-1 and Subset-2, which are identical for all three responses. Each time a new response is analyzed, Subset-1 and Subset-2 are kept identical to provide a first step at quantifying the variability of the response. Therefore, the content of the other subsets is dependent on the percentage contributions identified through Subset-1 and Subset-2.

Considering the results in Table 8, a large variation in variability of the response can be observed as Subset-1 becomes Subset-2 by replacing T_1 with T_8. When T_1 is included back in Subset-4, compared to Subset-2, a drop in variance is observed. As all subsets that include T_1 had a 1% percentage contribution from T_1 in the overall variability, it is feasible to conclude that T_1 is ineffective for the final distance-to-go.

From a physical stand point, it is reasonable to conclude that the thrust component T_1 exhibits relatively diminished effectiveness when compared to the thrust magnitudes at subsequent nodes. Notably, T_1 is positioned at the initial stages of the ballistic phase, wherein the trajectory of the booster is primarily

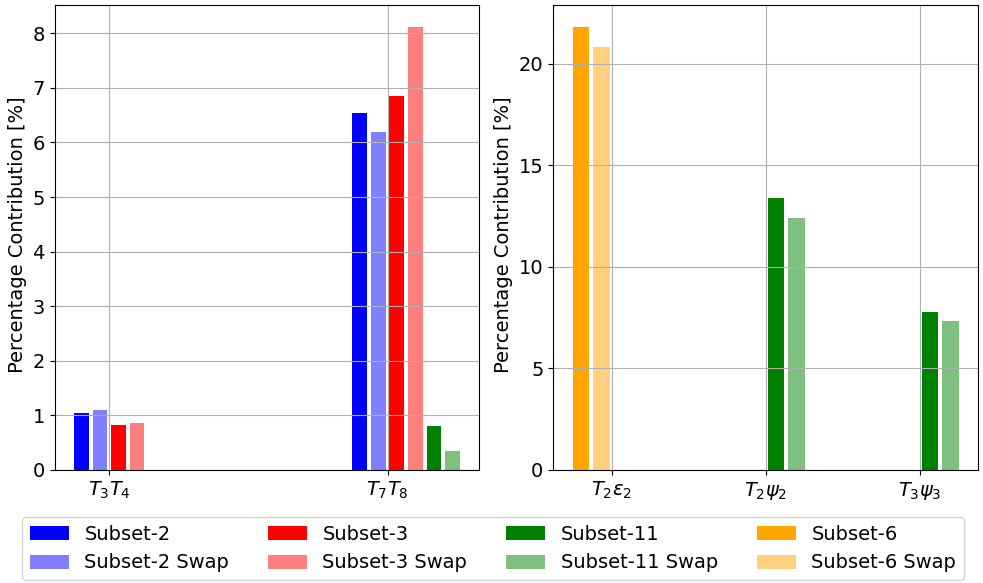

Figure 6. Percentage contribution of the thrust parameter interactions to the final distance-to-go across different subsets

dominated by the lift and gravitational force. To counteract the ballistic phase, the thrust force has to be sufficient enough to pull up the nose of the booster. The fact that T_1 is ineffective indicates that even with the maximum values, the capabilities of the propulsion system are not sufficient to deliver the forces to overcome the aerodynamic and gravity forces at the very beginning of the ballistic phase.

Subsequently, it becomes evident that the parameters T_2 and T_3 assume a significant role in shaping the response of final distance-to-go. Despite nodes 2 and 3 also being situated along the ballistic trajectory, they correspond to locations where the influence of lift forces is comparatively diminished due to the higher altitudes involved. Therefore, the generated thrust force can overcome the aerodynamic forces without any trouble. Finally from analysis of thrust magnitudes, it is identified that T_7 has a high percentage contribution to the distance-to-go. Since node 7 is one of the final nodes, right after the turn maneuver, it defines whether the leveled flight can be sustained by the booster.

The difference in the variability of Subset-11 and Subset-11 Swapped Column indicates that there are possible interactions that are confounded. Looking at the percentage contribution of T_7T_8 in Figure 6, a non-negligible influence on the response can be spotted. An interaction between T_7 and T_8 is plausible. When thrust is too high at T_7 more fuel would be consumed, causing a decrease in mass before reaching T_8. Note that the leveled flight is identified as an unaccelerated flight. Thus, as the mass is reduced to sustain a level flight, the thrust magnitude also has to be reduced at T_8. Else, an increase in the altitude would be observed as the normal thrust force would be more than the normal gravitational force.

An additional observation that can be drawn from Figure 6 is the decrease in the percentage contribution of T_7T_8, coinciding with the introduction of thrust azimuth angles. Referring back at Table 8, although the individual contribution of thrust azimuth angles is not significant, just like the elevation angles, they have a high contribution when they are coupled with the thrust magnitude. Potentially, the decrease in T_7T_8 when $T_2\psi_2$ and $T_3\psi_3$ are introduced could be linked to the fact that a strong thrust magnitude and azimuth couple could potentially induce an early turn maneuver. Due to the high altitudes at node 2 and node 3, a turn maneuver can be induced as long as sufficiently large thrust is introduced. As a result, the contribution of the T_7T_8 would drop since the final range to be covered would be much smaller compared to previous cases.

Prior to the simulations, it was expected to observe strong interactions between the thrust magnitude and thrust elevation angles. Especially for the highest contributing nodes, such as nodes 2, 3, and 7. On the contrary, the analysis of Subset-6 till Subset-10 concludes that only the $T_2\epsilon_2$ interaction is high, as depicted in Figure 6. Looking at the equations of motion:

$$m\frac{dV}{dt} = -D - mg\sin\gamma + T\cos\epsilon_T \tag{26}$$

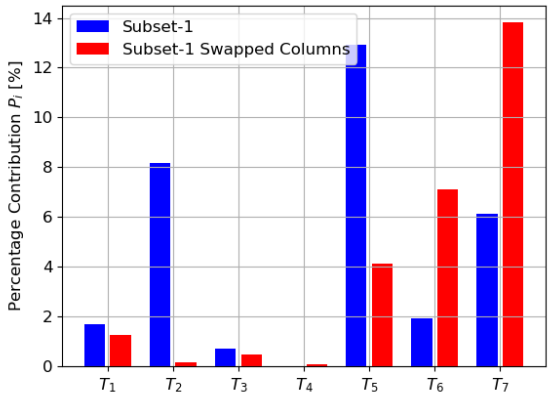

Figure 7. Percentage contribution of Subset-1

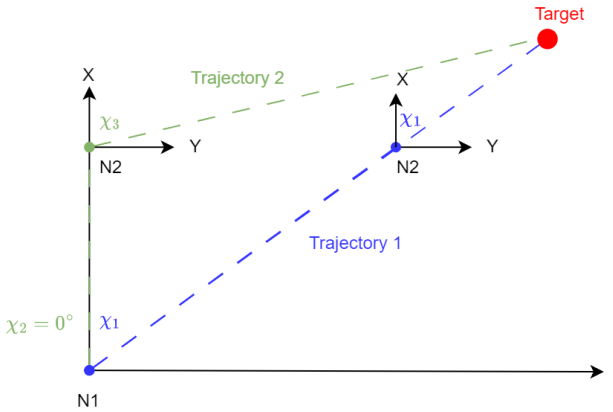

Figure 8. Example trajectories with two nodes and a target for explaining the heading angle change

$$mV\frac{d\gamma}{dt} = L - mg\cos\gamma\left[1 - \left(\frac{V}{V_c}\right)^2\right] + T\sin\epsilon_T \tag{27}$$

it can be observed that the thrust elevation contributes to the acceleration. However, only if the thrust magnitude is sufficiently high, the thrust elevation can assist with controlling the thrust vector and distributing the thrust magnitude in the desired axis. At node 2, the altitude is so high that the aerodynamic forces are almost insignificant. Therefore, within the thrust-magnitude range, the majority of the magnitudes yield a thrust force larger than the aerodynamic force. Meanwhile, although node 3 is also placed at a high altitude, it is a bit lower than node 2, therefore a decrease in the contribution of $T_3\epsilon_3$ can already be spotted as aerodynamic forces begin to rise again. Meanwhile, for the rest of the trajectory, even the highest thrust magnitude and thrust elevation couple are not the driving forces. Thus, they are not affecting the final distance-to-go as much as was suspected previously. This phenomenon continues until the mass is sufficiently reduced, such that the gravitational acceleration is smaller than the thrust acceleration. To cope with this and increase the effect of thrust elevation angle on the trajectory for controllability reasons, the maximum allowable thrust of the engine has to be increased.

C. Final Heading Angle

The final heading angle defines the direction in which the booster points at the final point of the trajectory. It is significant to keep the heading angle aligned with the target landing site as much as possible to also successfully meet with the TAEM conditions.

In contrast to the mean and standard deviation of the other two responses' subsets, the final heading angle subsets have a larger standard deviation than the mean, as shown in Table 5. This phenomenon in the response, combined with a small mean, suggests that outliers could be present in the data set as outliers introduce a disproportionate influence on the mean. Consider Subset-1, the corresponding standard deviation, and mean values suggest that certain $T_1 - T_2 - T_3 - T_4 - T_5 - T_6 - T_7$ combinations result in final heading angle values that are far from the bulk of responses, around the mean. Outliers are an indication of various things, one of these is the presence of strong interactions. To confirm this, the swapped column subsets and the individual contributions of the factors are analyzed in detail.

The results implies that the final heading angle is affected far more by the accumulative interactions between different thrust parameters, than other responses. To begin with, the analysis of Subset-1 and Subset-2 immediately showed a difference between the original subsets and the swapped column subsets. As depicted in Figure 7, the percentage contributions are not consistent regardless of the order in which the factors are assigned. Nevertheless, different thrust parameters are combined to obtain a better understanding of the phenomena. However, the analysis of each subset concludes that there are strong interactions between thrust parameters at different nodes. Especially the ψ and T contribute the most to the variation in the final

Table 5. Properties of selected fractional factorial subsets of the final heading angle

	Parameters	Mean	STD	Variance
Subset-1	$T_1 - T_2 - T_3 - T_4 - T_5 - T_6 - T_7$	0.6991	1.7015	2.8952
Subset-1 Swapped Column	$T_5 - T_2 - T_6 - T_4 - T_7 - T_1 - T_3$	0.4603	1.7858	3.1891
Subset-2	$T_2 - T_3 - T_4 - T_5 - T_6 - T_7 - T_8$	-0.0674	1.5822	2.5035
Subset-2 Swapped Column	$T_5 - T_7 - T_4 - T_2 - T_3 - T_6 - T_8$	0.1356	1.5096	2.2789
Subset-8	$T_5 - T_6 - T_7 - T_8 - \psi_5 - \psi_6 - \psi_7$	0.1323	1.5257	2.3279
Subset-8 Swapped Column	$\psi_5 - \psi_7 - \psi_6 - T_7 - T_5 - T_8 - T_6$	-0.1766	1.6109	2.5948
Subset-9	$T_1 - T_3 - T_5 - T_7 - \psi_1 - \psi_3 - \psi_7$	0.5987	2.0471	4.1907
Subset-9 Swapped Column	$\psi_1 - T_1 - \psi_3 - \psi_7 - T_3 - T_7 - T_5$	0.7421	1.9921	3.9693

heading angle. This complicates the analysis since a common trend cannot be spotted among the thrust parameters.

Although a conclusive result cannot be obtained, it is suspected that the interactions between the thrust parameters in the mid-range nodes, right after Phase 1, are significant. That is due to two main reasons. First of all, after Phase 1, the turn maneuver is induced. Therefore, the heading angle is changed with banking. During this phase, the heading angle could be more sensitive to changes in the thrust azimuth, since certain values could interrupt the heading angle change that was induced by the turn maneuver. Secondly, as was stated above, large differences can be observed between the percentage contribution of parameters at nodes 5, 6, 7, and 8. Meanwhile the variance across the original and swapped column subset shows a large variation in the variance as well, as shown by Subset-8 in Table 5. These differences indicate that not only the individual effect of the factors is significant, but also the interactions they have with other factors.

Although it is anticipated to observe a weaker relationship between nodes, as nodes are further apart, it is possible to encounter long-range interactions that propagate through time. Long-range interactions may impact the final heading angle, particularly with respect to ψ, given its substantial influence on the booster's flight direction throughout a flight. From a physical perspective, the effect of a wrong direction in one node could propagate, requiring several subsequent nodes for correction. An example is depicted in Figure 8, in which there are two distinct trajectories each with nodes, N1 and N2, and a target point.

N1 remains consistent in both trajectories, with varying initial heading angles. The first trajectory has a heading angle χ_1 which is aligned with the target point. Consequently, this trajectory implies that when the heading angle coincides with the target's heading angle from N1 onwards, minimal alterations occur in N2 to adjust the heading angle, as it remains χ_1 at N2. On the other hand, the second trajectory have an initial heading angle $\chi_2 = 0°$. This suggests that if the heading angle at N1 is different, large changes have to be performed at N2 to align with the target point, since $\chi_2 \neq \chi_3$. Consequently, the changes in N1 influence the values in N2. It is suspected to see more complex interactions, if the number of nodes are increased, as the data discussed above suggests.

VI. Trajectory Optimization

To enhance the understanding of the subject, the unpowered flyback booster trajectory is also simulated and optimized. During the first batch of the optimization, the final distance-to-go could only be optimized till a final distance-to-go of 3.5°, and the values showed no improvement when a local refinement was performed. As a next step, a comprehensive analysis on the energy state is conducted to assess the feasibility of the unpowered flyback booster in reaching the TAEM phase, which is defined to initiate around Mach 0.8-1.1 at an altitude of 7-10 km.[10] The findings suggested that the unpowered vehicle does not have sufficient energy to reach the TAEM phase from a final distance-to-go of 3.5°. This outcome was in accordance with the results obtained by FESTIP. Consequently, for the reference mission designed by FESTIP, the airbreathing engines were activated at the end of Phase 2.

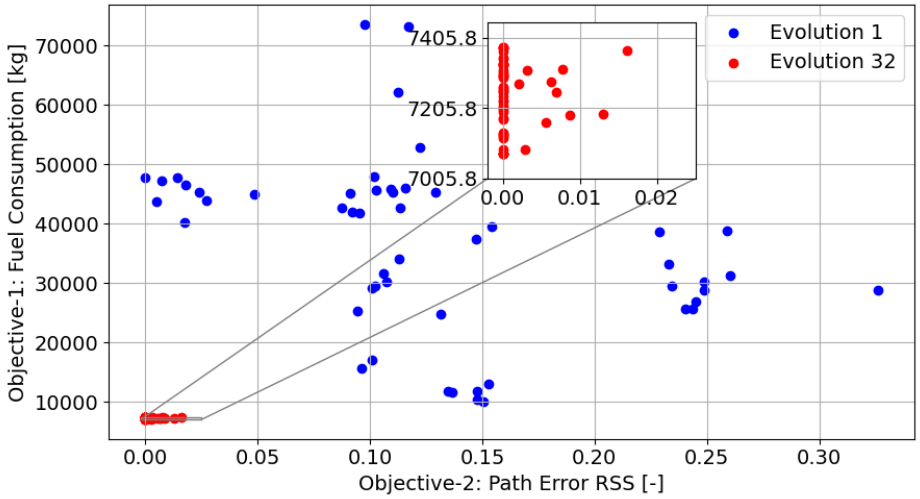

Figure 9. Objective space for the powered vehicle optimization with seed 42

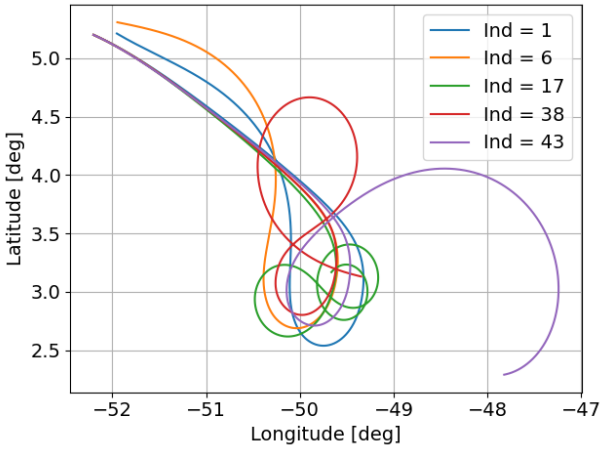

Figure 10. Latitude and longitude graph of random individuals from Evolution 1

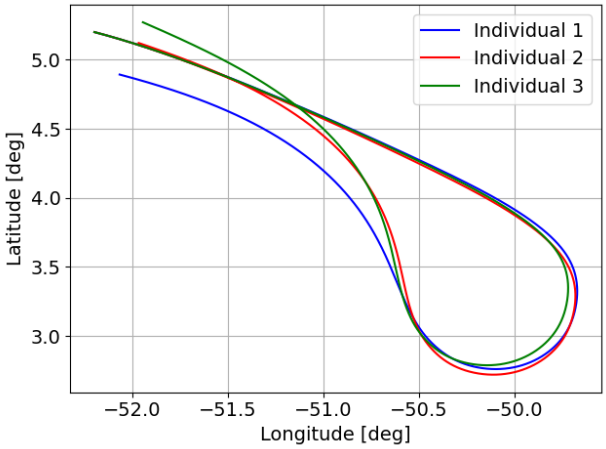

Figure 11. Latitude and longitude graph of chosen individuals from Evolution 32

A. Primary Optimization Results

To identify the most optimum trajectory in an efficient manner, the decision-variable range is adapted through the fractional factorial design method, which was identified in Section V. The Non-dominated Sorting Genetic Algorithm-II (NSGA-II) algorithm is used to optimize the flyback problem. The results are shown in Figure 9.

Individuals within the first population, Evolution 1, are diversely spread along the objective space, with relatively large values for the fuel consumption and path error RSS. Investigation of these values suggest that the raise in the fuel consumption is due to the penalty function. Thus, the final distance-to-go is significantly far from the desired final state. Considering the individuals in Figure 10 it can be seen that many of the trajectories are overshooting the target point before reaching a termination condition. This causes the vehicle to have large final distance-to-go values. Furthermore, due to the relatively long trajectories, the unpenalized fuel consumption values are also increased. Hence, the nominal value of unpenalized fuel consumption at Evolution 1 is around 10,000 - 20,000 kg, which is relatively large when it is considered that the booster mass is only 57,000 kg.

When Objective 2 is analyzed further, it was expected to observe violations in g-load and trim conditions due to the nature of the vehicle. However, when the values are analyzed, it is identified that the individuals

Table 6. Best individuals from Evolution 32 for seed 42

	Individual 1	Individual 2	Individual 3	Units
Fuel Consumption	7075.79	7380.12	7368.91	kg
Path Error RSS	0.0	0.0	0.016	-

in Evolution 1 only violate the g-load constraint. Therefore, every trajectory in the first population is trimmable. The powered vehicle has a fixed angle of attack profile, which could dictate that the trim condition is fixed. Although the angle of attack and Mach number are the two main parameters that influence the trimmability of a vehicle, as the thrust elevation angle changes it was expected to observe a change in the trim condition, perhaps even identify untrimmable trajectories. A further discussion on this topic is carried out in Section VII. Therefore, in Evolution 1 the only path constraint that is consistently violated is the g-load constraint.

As the optimization progresses, a significant shift in the objective space is observed. Three individuals are chosen for further inspection in Evolution 32. The first individual has the best Objective 1 and Objective 2, the second individual has the best Objective 2 but the worst Objective 1, and the final individual has the worst Objective 2 and a very high Objective 1. The objective values of each individual are presented in Table 6.

Looking at the latitude and longitude history of each individual in Figure 11, it is seen that the reason behind varying Objective 1 values is the fact that the termination conditions for Individual 2 and Individual 3 are reached later than for Individual 1. Consequently, a longer flight time caused the booster to consume more fuel. Individual 1 reaches the final distance-to-go without changing the final heading angle that is obtained from the turn maneuver. Thus a heading angle of $-70.4°$ is sustained till the final termination condition of $0.75°$ is reached. Note that the other two termination conditions, which are the lower altitude and velocity, are not reached. This indicates that the vehicle was able to sustain a leveled flight until the desired final distance-to-go is reached. Meanwhile, Individual 2 alters its heading angle to $-55.2°$ to meet with the main leg of the trajectory, which is the main difference of this trajectory from Individual 1. This extra maneuver is potentially causing the vehicle to burn more fuel. Meanwhile, Individual 3 overshoots the main leg and proceeds further until the final distance-to-go of $0.75°$ is reached. Both from Individual 1 and Individual 3, it can be concluded that the booster meets with the TAEM conditions and even has sufficient offset to perform a heading alignment cylinder (HAC) maneuver. Nevertheless, although all three trajectories almost seem identical, the longer two trajectories, Individual 2 and Individual 3, cause the vehicle to consume more fuel. This could indicate that perhaps the heading angle constraint should not have been relaxed, as a larger χ causes the vehicle to consume more fuel. Nevertheless, Individual 2 and Individual 3 could increase the fuel consumption in this fly-back trajectory at the expense of reducing the fuel consumption in the TAEM phase. To make a conclusive decision about that further research is required.

Upon investigating the values of Objective 2, it is identified that for Individual 3 only the g-load constraint is violated. To observe the g-load of the vehicle the components that contribute to the total acceleration are regarded. These are the aerodynamic acceleration, gravitational acceleration, and thrust acceleration. The point in which the g-load rises close to 3g, is the point after the peak altitude of Phase 1, as the booster dives deeper into the atmosphere. Due to the nature of this maneuver, the aerodynamic acceleration is rising at this point. The aerodynamic acceleration is dependent on the value of the lift and drag. Since the angle of attack profile of the powered vehicle is fixed, across different trajectories the lift and drag profiles are almost fixed as well. However, since the thrust force affects the trajectory there could be changes in other components of the lift and drag, such as the velocity and the density. Therefore, an increase in total acceleration is observed, due to combination of the thrust and aerodynamic forces.

Furthermore, as was mentioned previously, the same phenomenon can be observed for the individuals that had a high Objective 2 in Evolution 1. As the vehicle has direct control over the thrust magnitude and direction, the thrust force is adapted at each evolution to obtain a trajectory with a non-violated g-load constraint.

Upon considering all the discussions above, it is concluded that Individual 1 is the most optimum solution. At this point, the optimization is performed using a booster mass of 57,000 kg. This was the wet vehicle mass set by FESTIP. However, during their calculations and trajectory simulation, FESTIP only used fuel for Phase 3. Meanwhile, Phase 1 and Phase 2 are only performed by aerodynamic means. Thus, it could be

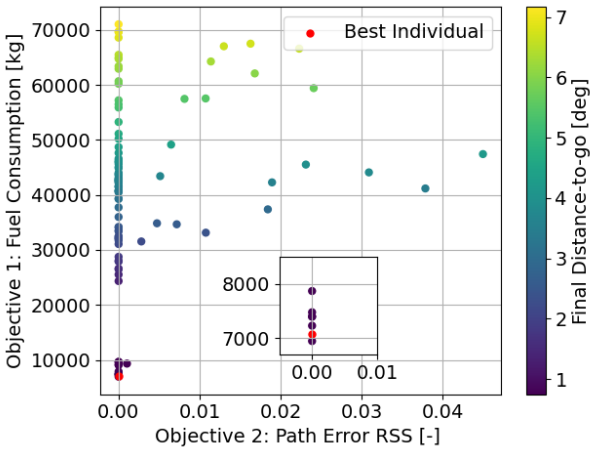

Figure 12. Powered optimization local refinement with seed 42

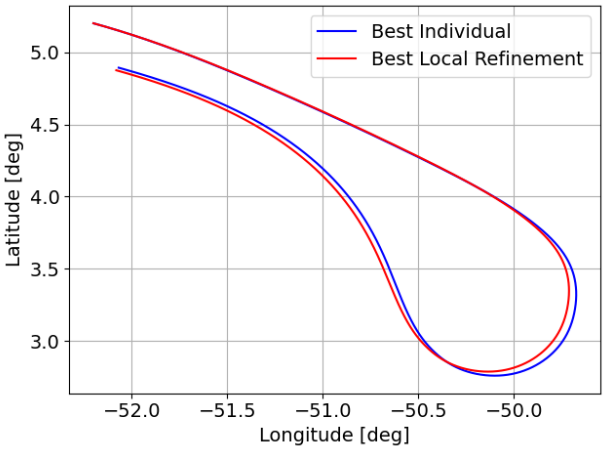

Figure 13. Latitude and longitude history of the best optimization and local refinement individuals

that the initial fuel set by FESTIP is insufficient and the vehicle may require more. The mass properties of FSSC-16 suggest that FESTIP has calculated to have a fuel consumption of 7,000 kg, in which 5,000 kg is for the fly back and 2,000 kg is the reserved fuel. The optimum solution yields that the required fuel mass is 7,076 kg. The difference between the two calculations is around 76 kg, which corresponds to a difference of 1.1%. Not only is this difference significantly small, such that it is within the allowable limit for an error in mission design (around 10%-20% depending on the design phase), but it also does not affect the trajectory very much.[7,12]

B. Local Refinement Results

Given the highly favorable outcome derived from the optimization process, it is imperative to undertake a comprehensive verification to ascertain the optimality of the obtained solution. Consequently, local refinement is used to fine-tune the solution by exploring the objective space at the vicinity of the optimal solution. Out of 100 individuals, there is a single individual that performed better than the solution obtained by the optimization algorithm, as depicted in Figure 12. The latitude and longitude history comparison of both individuals is presented in Figure 13. It is observed that the main difference is the radius of the turn maneuver, which could save 130 kg of fuel for the best individual of the local refinement process.

The primary findings of the local optimization indicate the need to perform an iteration on the optimization to enhance the optimal solution. This can be accomplished through the application of two distinct optimization methodologies. First, a local optimizer can be implemented using the best individual, Individual 1, to explore the design space around. A second method is using the current global optimizer. However, if the optimization is re-initiated using an initial point that is close to a local minimum, which could be Individual 1 in this case, the algorithm converges towards the same region. When the optimization is initiated with a good initial guess, NSGA-II starts to search from a point that is already the optimal region in the design space. The diversity in the NSGA-II algorithm is preserved through non-dominated sorting and crowding distance. Nevertheless, when the initial guess is a non-dominated solution, which is Individual 1, the NSGA-II algorithm cannot escape to other design spaces.

Accordingly, a slight improvement in the optimal solution can be obtained due to crossover, mutation, and randomness of the algorithm. Nevertheless, it is expected to observe that the new optimal solution is significantly close to Individual 1. To cope with this problem, the optimization process has to be adapted to ensure that a different design space is discovered. This is achieved by using a different initial guess and by adding the best individual of the local refinement to the initial population. When the NSGA-II algorithm encounters an initial guess that is superior to the previously converged solution, the search is guided towards this new region of the design space. Consequently, the offspring that follows this initial guess also has an improved objective value. Finally note that the decision-variable range is adapted, such that the range is $\pm 10\%$ of the best individual of the local refinement. By doing so, the design space obtained by the local

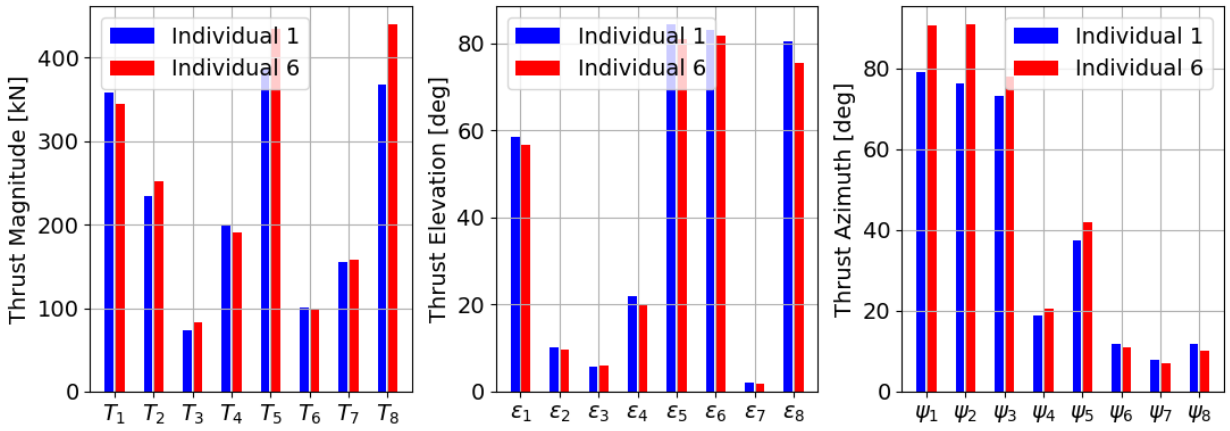

Figure 14. Comparison of the profiles of Individual 1 and Individual 6

refinement is explored further.

It is worthwhile to mention that the best individual of the iteration is identified as Individual 6. Observing the contents of Figure 14, it is evident that the largest difference in thrust parameters is among the thrust magnitudes. T_3, T_5, and T_8 has varied recognizably among Individual 1 and Individual 6. In fact, the values of T_5 and T_8 exceed the maximum allowable thrust limit of 400 kN.

Nevertheless, both individuals have the same fuel rate, which is 3.70 kg/s. Since Individual 6 reaches the desired point in a shorter duration, it also consumes less fuel compared to Individual 1. Note that, the FESTIP study did not have a definitive engine selection for FSSC-16, as they had a pool of three different engines. Thus, it would be recommended to select an engine that has only 10% more, thus 440 kN, than the current maximum allowable thrust. This would allow the vehicle to save an additional mass of 615.0 kg. However, since the current engine lacks the enhanced thrust capability, Individual 1 is confirmed again to be the optimal trajectory result.

VII. Sensitivity to Design Parameters

A. Reserved Fuel Analysis

The optimum trajectory suggests that the required fuel mass is 7,076 kg. This was only 1.1% more than what FESTIP had calculated to use for the return trajectory taking the reserved fuel into consideration as well. To study the sensitivity of the optimum trajectory to variations in mass, the optimum thrust parameters are utilized to simulate a trajectory with a new vehicle wet mass of 57,076 kg. Upon visual examination of Figure 15, it is observed that the booster can still follow the optimum trajectory. Although a clear explanation is not provided, it is plausible that FESTIP has factored in the allocation of 2,000 kg of reserved fuel in their calculations, considering the potential for an entirely powered trajectory throughout the mission.

Based on the preceding finding, an analysis is conducted to assess the feasibility of adding extra fuel to the current wet mass of 57,076 kg while maintaining adherence to the optimal trajectory. As depicted in Figure 15, when a reserved fuel of 2,000 kg or 1,000 kg is added, the booster deviates from its optimum trajectory. This suggests that the trajectory is sensitive to booster mass and can tolerate around 1% change, since 500 kg of fuel did not deviate the trajectory significantly. When the mass of the booster is increased, the required thrust to reach the desired conditions is also increased. Especially at the end of the trajectory, when the booster has to perform a pull-up maneuver by overcoming the gravitational force. As the required thrust is increased, the propulsion system expels more fuel.

B. Decision Variables Range Analysis

Analyzing the decision variables' effect on the design space has been the primary aim of this research. It was identified that certain parameters have a larger influence on the trajectory than others. Accordingly, the ranges of the decision variables are adjusted to drive the optimization process toward the desired solution

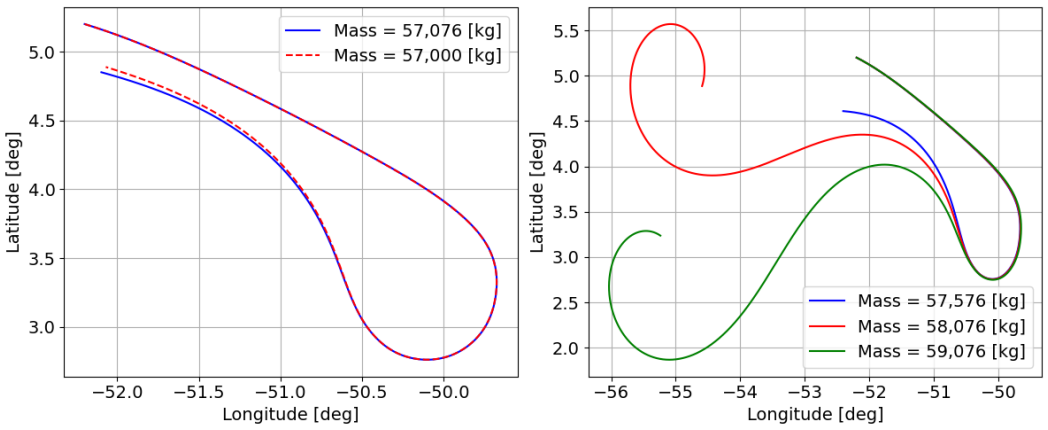

Figure 15. Optimum trajectory with different booster masses

Table 7. Change in the optimal decision variables

Type	Changed Variables
Adapted Range	None
Semi-adapted Range	$T_3 - T_7 - \psi_7 - \psi_8$
Full Range	All

space. To evaluate the effectivity of this action, a sensitivity analysis is conducted, involving comparison of optimization solutions generated using three distinct set of ranges for the dependent variables.

As identified in Table 7. the adapted range set is the one that is used while solving the optimization problem. The semi-adapted range is a range in which the values of $T_3 - T_7 - \psi_7 - \psi_8$ are changed. T_3 and T_7 are adapted to have higher upper limit of 400 kN, while $\psi_7 - \psi_8$ adapted to have a higher lower limit of 30°. The importance of T_3 and T_7 was highlighted as a result of the fractional factorial design analysis. Particularly, the low values of T_3 identified to be a contributing factor, given that it represents the point at which the vehicle starts to generates lift. Encountering excessive thrust at this point could cause vehicle to skip from the atmosphere.

Furthermore, the lower limit of ψ_7 and ψ_8 are adjusted to be 30°, because it was observed that during the optimization, using the Adapted Range set, these final values are consistently around 15° - 25°. It is noteworthy to highlight that the value of the elevation angle at the final nodes is not changed. It is evident from the design-space exploration that ϵ_7 and ϵ_8 have a substantial influence on the flight-path angle, thereby effecting the final distance-to-go. Finally, in the Full range set, no decision variable is constrained, giving a sufficiently large solution space to the optimizer.

In Figure 16 , the progress of Objective 1 with each evaluation is depicted, in which all three optimizations converge to a solution. Nevertheless, a distinct difference between the convergence speed can be identified. Therefore, the figure suggests that the convergence speed of the solution is affected by the decision variable range. Comparing the initial and the final value of Objective 1, it is observed that the full range has the largest change in the value of Objective 1. Meanwhile, both the Semi-adapted and the Adapted range show convergence characteristics around the 20^{th} evolution. However, it is significant to note that fast convergence does not necessarily indicate that the converged value is the optimal solution or a feasible solution at all.

In Figure 17 the latitude and longitude histories for the best Objective 1 individual of all three trajectories are depicted. While the full range and adapted range optimizations could reach the vicinity of the desired final distance-to-go, the semi-adapted range optimization failed to do so. Instead, the vehicle gets stuck in the turn maneuver. Consequently, a spiral motion is observed. Since the range of the thrust azimuth angle at the last two nodes is adapted, the optimizer obtained values around the higher end of the range, rather than the lower end. The corresponding thrust azimuth angles are reported in Table 8. When the large azimuth angle is combined with a high thrust magnitude at the last node, which is around 400 kN for all three

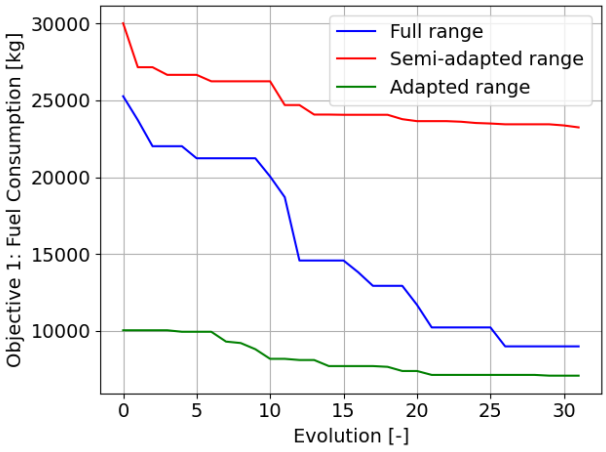

Figure 16. Best individual for Objective 1 at each evolution with seed 42

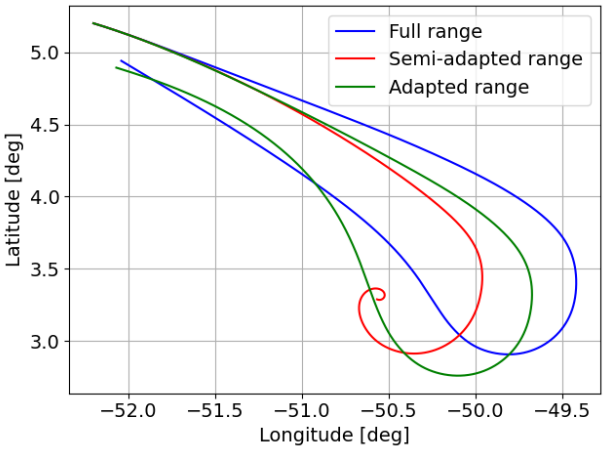

Figure 17. Latitude and longitude of the best individual at the final evolution with seed 42

Table 8. Change in the azimuth angle of the last two nodes across different ranged optimizations

	Full Range	Semi-adapted Range	Adapted Range	Units
ψ_7	18.0	57.51	8.0	deg
ψ_8	24.19	79.98	11.66	deg

individuals, the booster has an excessive side force. As the side force increased, the booster could not get out of the turn maneuver and got stuck in a spiral motion. Therefore, partly changing the decision variable, without properly accounting for the decision variable range causes the algorithm to converge towards a local optimum, which is significantly less feasible than other local optima.

It is significant to note that both the adapted range and full range converge towards relatively close values. Since the full range optimization shows a large decreasing trend over various evolution indices, it is possible that within a few more evolutions, the objective may drop further. In that case, a trade-off has to be performed. It is always a possibility to use the full decision variable range, especially when a design space exploration is not or cannot be performed. However, this may result in a higher computational time and a slower convergence speed. Meanwhile, the largest difference between the full range and adapted range optimization is in the thrust azimuth profile. Although the range of the thrust azimuth in the first node is not adapted, it can be seen that for a full range optimization, the optimizer found a much lower value. For the adapted range optimization $\psi_1 = 79°$ and for the full range optimization $\psi_1 = 29°$. The result suggests that, technically the booster is also possible to obtain a trajectory that can reach the final distance-to-go with a lower azimuth angle at the first node. However, this is at the expense of a larger fuel consumption, the turn maneuver is initiated a lot later in the trajectory (see Figure 17).

The decision variable range significantly influences the optimization process by directing it toward a more attainable solution space. Despite having the same number of individuals and evolutionary iterations, the Adapted and the Semi-adapted range optimizations reached convergence ahead of the Full-range optimization. The latter not only exhibited later convergence but also required a longer computational time, primarily due to the initial exploration of a considerably larger design space. This underscores the importance of constraining decision-variable ranges to ensure a fast optimization convergence.

C. Bank Angle and Lateral Stability Analysis

The results of the FFD concluded that the last two nodes are significant actors that shape the trajectory. In case the thrust vector control is insufficient at these nodes, the vehicle cannot sustain a leveled flight. Accordingly, the desired final distance-to-go cannot be reached. Upon arrival of the last two nodes, the booster terminates the turn maneuver (Phase 2) and initiates Q leveled flight (Phase 3). At this point, due to magnitude of the aerodynamic forces on the vehicle, the flight dynamics encountered by the booster is

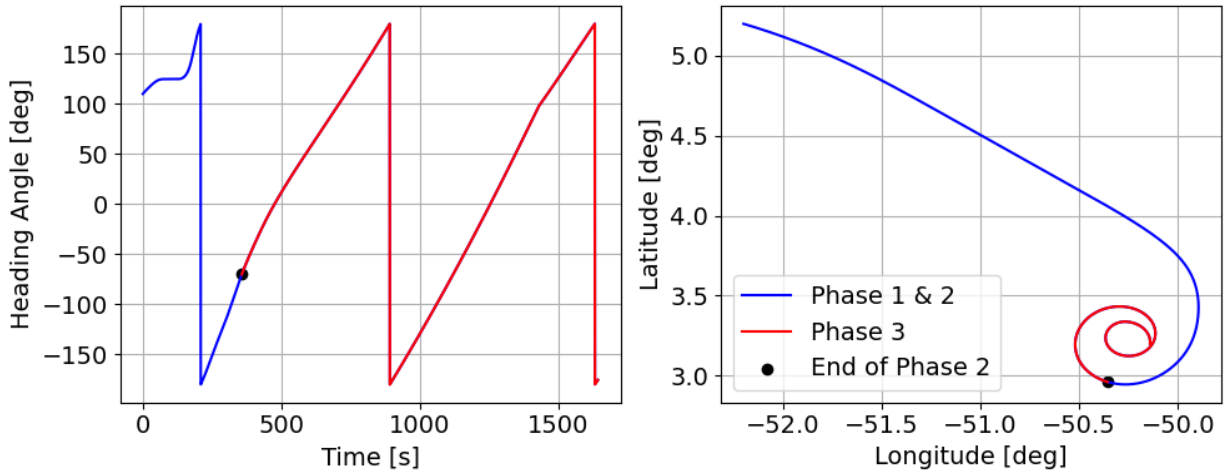

Figure 18. Visualization of the spiral motion due to the changed bank angle profile

similar to the ones of an aircraft. Consequently, a pronounced coupling between the yaw and roll moment can be addressed. This phenomenon is avoided by actively controlling the bank angle alongside the heading angle, as was previously identified in Section IV.

The primary objective was to investigate the impact of this control coupling on the trajectory. Given that a perturbation in this control coupling has the potential to induce instability within the system, the optimum bank angle profile is intentionally disturbed.[2] Subsequently, the bank angle profile of the unpowered flyback booster is fed to the simulation.

The results are depicted in Figure 18. In Phase 3, the trajectory is suffering from a spiral motion, which is an aperiodic eigenmotion that has the bank angle as its main driving parameter. Characteristics of the spiral motion dictate an uncoordinated flight due to undesired side force. In this scenario, an uncoordinated flight is characterized by an excessive or inadequate control inputs, encompassing the deflection of rudder, ailerons, or thrust azimuth. Consequently, at the end of Phase 2, the thrust azimuth induces a large side force, causing the vehicle to be stuck in the turn. As observed from the alternating heading angle illustrated in Figure 17, the side force gives rise to a spiral motion, which is a phenomenon concurrently recognized as thrust-induced yaw motion. The subsequent analysis concluded that the active control of the bank angle profile is imperative for the preservation of lateral stability.

D. Thrust Elevation and Trimmability Analysis

The booster is simulated such that there is an active trim logic, as long as an aerodynamic database is provided. The presence of a propulsion system complicated the trim logic, as the thrust force also contributes to the pitch moment when $\epsilon = 0°$. When there is a thrust elevation angle, the force is distributed along the longitudinal axis of the vehicle. In certain cases, the additional force could affect the trimmability of the vehicle. To observe whether the thrust force influences the trimmability of the vehicle, the optimum trajectory is compared to a trajectory in which the thrust-elevation is zero for the entire flight.

The graphs in Figure 19 indicate that the vehicle is trimmable for both thrust elevation profiles. At the beginning of the trajectory, a small difference in the deflection of the body flap can be spotted. This difference is solely dependent on the force T_{Z_B}. Since this time incidence, corresponds to the ballistic flight to a certain degree, the aerodynamic forces are ineffective. Therefore, the pitch moment is driven by the thrust force in the Z_B axis, which is calculated using the thrust magnitude T and sinus of the thrust elevation angle ϵ_T. This indicates that the T_{Z_B} is large when the thrust elevation angle is far from zero. Consequently, the thrust force contributes more to the pitch moment and forces the body flap to deflect more to correct for this induced pitch moment. Therefore, the body flap with zero thrust elevation followed a much more constant and lower deflection angle profile. The zoomed-in graph is depicted in Figure 20. Afterward, during Phase 2, which roughly corresponds to 200-500 seconds, both the aerodynamic and thrust forces are contributing to the pitch moment. As the two forces are combined the uncorrected pitch moment became more negative,

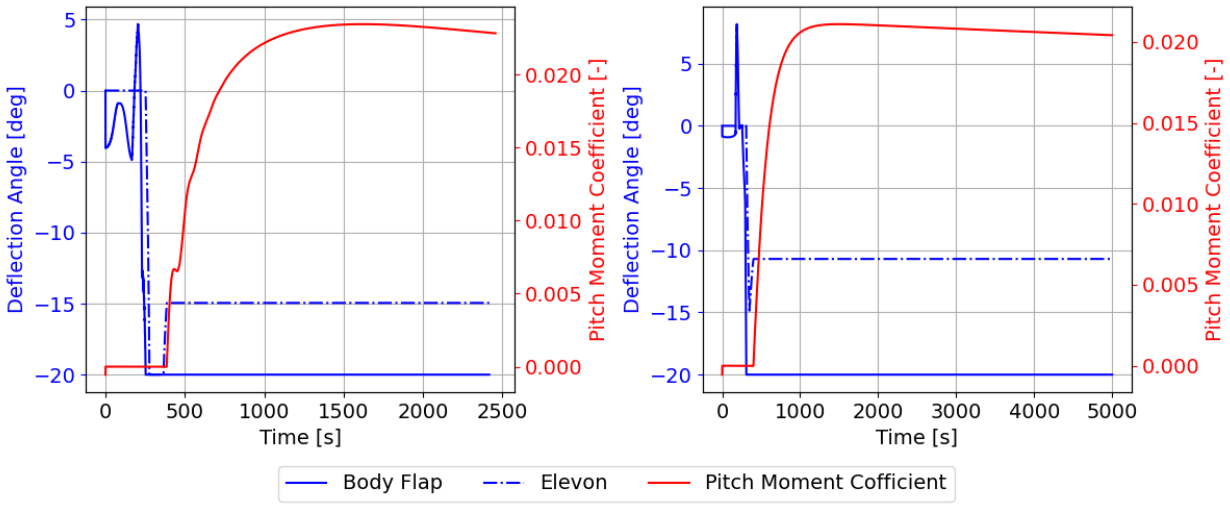

Figure 19. Optimum trust elevation profile (left) and $\epsilon_T = 0°$ profile (right)

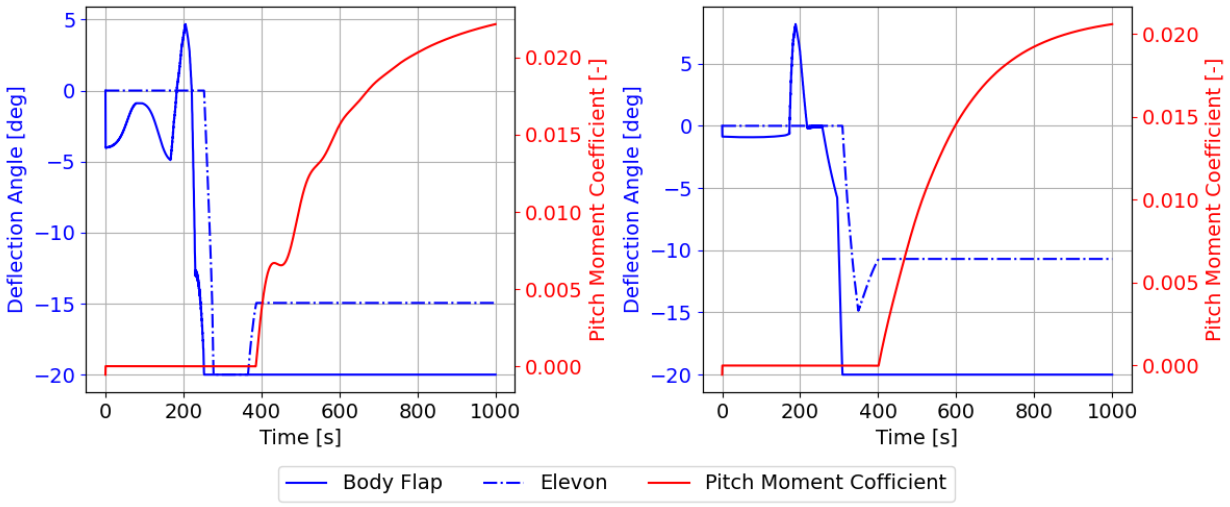

Figure 20. Zoomed in figure for the optimum trust elevation profile (left) and $\epsilon_T = 0°$ profile (right)

consequently the body flap is deflected negatively to induce counteracting positive pitch coefficient. Note that as the thrust force is located aft of the center of mass, it induces a negative pitch moment and pushes the nose of the vehicle down.

The results suggest that the change in the thrust elevation angle has a minor influence on the trim of the vehicle in Phase 1 and Phase 2. However, to observe whether or the trim and thrust force sustain this weak relationship, the change in the moment coefficient in Phase 3 is observed. Considering the trim graphs in Figure 19 again, although C_m for the optimum thrust elevation profile is a bit larger, no considerable change in C_m can be observed from 600 seconds onward. Thus, for the entire flight profile, a change in the thrust elevation angle has a minor influence on the deflection angles. Therefore, the thrust elevation angle does not severely affect the trimmability of the vehicle.

It is significant to note that the degree of correlation between thrust and trim is intricately tied to two characteristics of the vehicle design. First is the distance between the center of thrust (CoT) and center of mass (CoM). Whereas, the second it he thrust magnitude. By increasing both of these values the influence of thrust induced pitch moments can be increased. Consequently, a more pronounced association between trim and thrust is identified, requiring a larger deflection of the aerodynamic surfaces to offset the increased

contribution of thrust-induced moments.

Nonetheless, in the presence of a true decoupling between trim and thrust, it would mandate that the deflection of the control surfaces is identical, irrespective of the thrust condition. This decoupled characteristic of thrust and trim holds a substantial advantage for the booster's control system. The longitudinal stability of the booster is solely dependent on α, M, and control surface deflections, δ. When the two variables are decoupled, the control system only accounts for these variables to sustain the stability and discard the elevation angle. As there are fewer variables, the control system design can be more efficient. Certain studies have simulated a decoupled longitudinal flight for a short takeoff and landing (STOL) aircraft.[4] As a result, it has been identified that such vehicles have better-handling qualities, which is a desirable behavior for a precise approach and landing.

VIII. Conclusions and Recommendations

In this paper, the optimum trajectory of a flyback booster is studied, with the overarching aim of achieving efficiency in obtaining the optimal solution. This research is focused around conducting a comprehensive design space exploration by utilizing methods that are varied from a one-at-a-time simulation to a fractional factorial design.

Nodes 2, 3, 7, and 8 are identified as critical points influencing fuel consumption. It was identified that the thrust magnitudes have a direct influence on fuel consumption. Whereas, the thrust elevation and thrust azimuth angles have an indirect influence, since these can affect the duration of the flight. During Phase 1, due to a lack of aerodynamic control, the ballistic flight causes the vehicle to fly further away from the target, which also increased the flight time. By altering the thrust magnitude at this point, which are T_2 and T_3, the duration of the ballistic flight was adjusted. In the meantime, inadequate control of T_7 and T_8 can result in insufficient force to to sustain leveled flight. Consequently, these nodes show importance for the fuel consumption and final distance-to-go. Whereas, the results of the final heading angle showed that the heading angle at the last instant may suffer from accumulated interactions along the trajectory, it was significantly difficult to identify a coherent behavior. However, a strong relationship could be observed for the midpoint nodes, which are nodes 5, 6, 7, and 8.

Upon identifying the importance of a comprehensive design space exploration, an optimization is performed. The converged solution demonstrated a flight with a final distance-to-go of 0.75° consuming only 7076 kg of fuel, which is only 1.08% more fuel than what is consumed by the FESTIP mission.

The validity of the optimum response is assessed by a set of sensitivity analysis. Especially, the results obtained from optimization of three distinct set of decision variables confirmed the intricate relationship between the variables and responses. Consequently, the optimum trajectory is highly sensitive to changes in the decision variables, yet can endure changes in mass properties until a certain level.

For future studies on trajectory design, it is recommended to repeat the design-space exploration and optimization process employing higher computational power. Increased computational power facilitates the implementation of a Resolution V fractional factorial design to observe the percentage contribution of each decision variable without any confounding. Given the complex nature of a flyback trajectory problem, the optimization was limited by the computational power. Hence, it is suggested to repeat the optimization process using larger batches, such as more individuals and more evolutions. Such a study would validate that the obtained solution is not limited by the number of evolutions and individuals, and it is indeed the global optimum.

Finally, it remains to be studied what the flyability of the optimum trajectory is. During the optimization process, the path and control constraints were implemented to move the design space toward more realistic trajectories. However, there are unaccounted factors that should be assessed to identify whether or not the vehicle can perform the flight in reality. Two main examples of these factors are a hardware assessment, and a stability and controllability analysis.

References

[1]Daimler-Benz Aerospace , "FSSC-16 Conceptual Launcher Design - Evaluation & Synthesis", ESA, Internal FESTIP Document, 1999.

[2]Day, R. E., "Coupling dynamics in aircraft: A historical perspective", California, National Aeronautics and Space Administration, 1997.

[3]Dujarric, C. , "Possible Future European Launchers– A Process of Convergence", ESA, *Third European Symposium on Aerothermodynamics for Space Vehicles*, Noordwijk, The Netherlands, November 24-26, 1998.

[4]Feinreich, B., Seckel, E., & Ellis, D. R. "In-flight simulation study of decoupled longitudinal controls for the approach and landing of a stol aircraft", USA, National Aeronautics and Space Administration. 1977.

[5]Fowlkes, W. Y., & Creveling, C. M., "Engineering methods for robust product design using taguchi methods in technology and product development", Addison-Wesley Publishing Company, 1995.

[6]Hanson J., "Advanced guidance and control project for reusable launch vehicles", AIAA, *AIAA Guidance, Navigation, and Control Conference and Exhibit*, Oslo, Norway, August 14-17, 2000.

[7]Hayhurst, M., Bitten, R., Judnick, D., Hallgrimson, I., & Youngs, M. (2016). "Historical Mass, Power, Schedule Cost Growth for NASA Instruments Spacecraft", Symposium Presentation.

[8]Mooij, E., "The Motion of a Vehicle in a Planetary Atmosphere (LR-768)", Delft University of Technology, 1994.

[9]Mooij E., "Aerospace-Plane Flight Dynamics: Analysis of Guidance and Control Concepts", Ph.D. Dissertation, Delft University Press, Delft University of Technology, Delft, The Netherlands, 1998.

[10]Naftel, J. C., & Powell, R. W. "Analysis of the Staging Maneuver and Booster Glideback Guidance for a Two-Stage, Winged, Fully, Reusable Launch Vehicle", Virginia, National Aeronautics and Space Administration, 1993.

[11]Spillenaar-Bilgen, J., "Global Ascent Trajectory Optimization of a Space Plane", (Master's thesis), Delft University of Technology, the Netherlands, 2017.

[12]SRE-PA & D-TEC staff. "Margin philosophy for science assessment studies", [Document], 2012.

[13]Tetlow, M. R., Schöttle, U. M., Schneider, G. M., "Comparison of glideback and flyback boosters", Journal of Spacecraft and Rockets, 2001, p. 752–758.